



Sound of effervescence

Mathis Poujol , Régis Wunenburger , François Ollivier,

Arnaud Antkowiak , and Juliette Pierre *

Sorbonne Université, CNRS, Institut Jean le Rond d'Alembert, F-75005 Paris, France



(Received 12 June 2020; accepted 3 December 2020; published 19 January 2021)

Capillary bubbles burst at a free surface following a rapid sequence of events occurring at different length scales and timescales: hole nucleation, fast retraction of the micron-thick liquid film in a few microseconds preluding the much slower overall collapse of the millimeter-sized bubble in a matter of milliseconds. Each of these steps is associated with unsteady fluid forces and accelerations, and therefore with sound radiation. In this experimental study we focus on the airborne sound generated during bubble bursting. Investigating the physical mechanism at the root of sound emission with the help of synchronized fast imaging and sound recordings, we quantitatively link the film retraction dynamics with the frequency content of the acoustic signal. We demonstrate that, contrary to a Minnaert resonance scenario, the frequency here drifts and increases, consistent with a Helmholtz-type resonance of the cavity being more and more opened as the thin film retracts. We propose as an extension a simple model based on a collection of drifting Helmholtz resonators capturing the main features of the fizzing sound of an effervescing beverage.

DOI: [10.1103/PhysRevFluids.6.013604](https://doi.org/10.1103/PhysRevFluids.6.013604)

I. INTRODUCTION

The crackling and fizzing sound of a freshly served glass of champagne is a matter of common experience [see Fig. 1(a)]. While there is little doubt that the sound originates from the bursting of capillary bubbles, the physical mechanism and overall picture of sound emission remains still somewhat unclear. In this work we propose to combine high-speed imaging with synchronous acoustic signal recordings in order to decipher the link between the fluid dynamics of bubble bursting and acoustic emission, and to pinpoint the physical mechanism responsible for the sound of effervescing beverages.

A typical acoustic signal emitted in the air during 1 s by an effervescent glass of champagne is shown in Fig. 1(c) and a 5 ms duration part of it is shown in Fig. 1(d). It displays a succession of sine-like short emissions (tone bursts). Processing the images of the liquid surface synchronized with the acoustic signal shown in Figs. 1(e)–1(h) reveals that a tone burst is emitted concomitantly with a collapsing bubble event occurring at the liquid surface. Further, the Fourier spectrum of the overall fizzing sound presents a striking similitude with that of a single bursting event [Fig. 1(i)], thereby strongly suggesting that the crackling sound of a glass of champagne merely results from a superposition of tone bursts emitted by single bubble bursts.

Champagne bubbles have been intensively studied [1–4]. Champagne and more generally sparkling beverages are saturated with CO₂, and their effervescence usually originates from the nucleation of bubbles on the glass wall. After detaching from their nucleation sites whose size can be as small as 1 μm, bubbles grow in size due to gas diffusion during their rise to the liquid surface.

*juliette.pierre@sorbonne-universite.fr

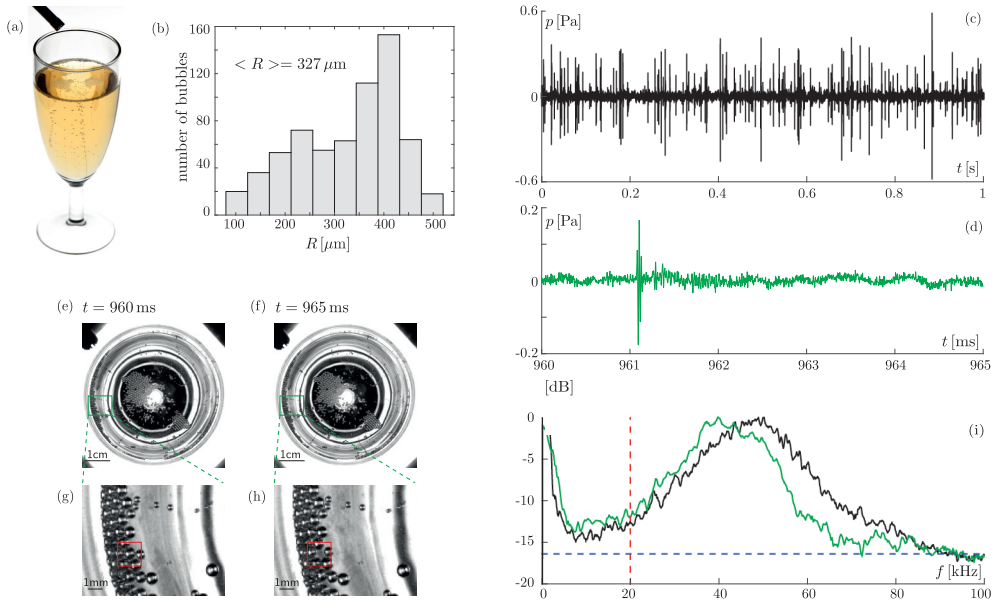


FIG. 1. Simultaneous acquisition of the airborne sound emitted by champagne in a glass and of a movie of the liquid surface viewed from the top. (a) Picture of a glass of champagne showing the microphone placed a few centimeters above the glass edge. (b) Histogram of the bubble radii extracted from a picture of the liquid surface at time $t = 960$ ms (average radius $\langle R \rangle = 327 \mu\text{m}$). (c) 1 s duration time history of the acoustic pressure high-pass filtered with a 50 Hz cutoff frequency and a sampling frequency of 500 kHz. (d) 5 ms duration part of the signal centered on a single emission event occurring at $t = 961$ ms. (e–h) Top view pictures of the liquid surface acquired at 200 fps using a high-speed camera synchronized with the acoustic signal acquisition. Pictures (e, f) and the enlargement of their framed part (g, h) evidence the disappearance of one bubble inside the red frame between $t = 960$ ms and $t = 965$ ms. (i) Acoustic spectra of the 1 s duration acoustic recording (c) (black curve) and of its 5 ms duration enlargement (d) (green curve). The blue horizontal dashed line indicates the noise level, and the vertical dashed line indicates the limit between the audible domain and the ultrasound domain.

At the surface where they ultimately collapse, their equivalent radius R , defined as

$$R = \left(\frac{3V}{4\pi} \right)^{1/3}, \quad (1)$$

where V is the bubble volume, ranges between $100 \mu\text{m}$ and $500 \mu\text{m}$, as shown in Fig. 1(b) [5]. In contrast with the extensive knowledge on the physics and chemistry of effervescence [1,2], only one study dedicated to the acoustic emission of champagne could be identified, in which the sound was related to the bubble size distribution [6].

The Bond number is the dimensionless quantity measuring the relative contribution of gravity and capillarity to the bubble shape: $\text{Bo} = (R/\ell_c)^2$, where $\ell_c = (\sigma/\rho_l g)^{1/2}$ is the capillary length (ρ_l is the liquid density, σ the liquid surface tension, and g the gravity acceleration). For champagne bubbles, $\ell_c = 2.2$ mm (see Table I), which results in $\text{Bo} \ll 1$ (for our experiments Bo falls in the range $[2; 50] \times 10^{-3}$) and thus in nearly spherical bubbles. We also note that champagne usually contains surfactant molecules [4] at low concentrations. In this paper we therefore study the sound radiated in the air by single capillary bubbles collapsing at the surface of both a pool of tap water and of water-surfactant solution (whose properties are given in Table I), the latter being used as a proxy for champagne to build an understanding of champagne sound emission.

TABLE I. Properties of the liquids and gases used in this work at 22°C.

Liquid solution	Density ρ_l (kg m ⁻³)	Viscosity μ (mPa s)	Equilibrium surface tension σ (mN m ⁻¹)	Capillary length ℓ_c (mm)	Gas	Density ρ_g (kg m ⁻³)	Celerity c (m s ⁻¹)
Tap water	10 ³	1	72	2.7	Air	1.2	345
SDS at 2 g L ⁻¹ + distilled water	10 ³	1	35	1.9	Air	1.2	345
Champagne (from Ref. [4])	992	1.6	48	2.2	CO ₂ (from Ref. [7])	1.8	267

Floating capillary bubbles are almost entirely submerged and are separated from the atmosphere by a thin liquid film. Mechanical equilibrium implies that the bubbles are over-pressurized by the Laplace pressure $\Delta P \sim 2\sigma/R$. Due to gravity drainage and capillarity suction, the film becomes thinner and thinner and finally bursts, as sketched in Figs. 2(a) and 2(b) and shown in Fig. 2(c). The film bursting leads to the sudden release of the internal pressure, which triggers the bubble collapse; see Fig. 2(d). High-speed side views of capillary air bubbles collapsing at the surface of a water pool reveal that this event lasts a few milliseconds and involves several steps. First, the liquid film breaks and retracts over a typical 100 μ s duration, as shown in Fig. 2(c). The cavity collapse occurs over a larger timescale, typically a couple of milliseconds, as shown in Fig. 2(d). Eventually the cavity reverses and a liquid jet is ejected, possibly rupturing into droplets and/or aerosols. These hydrodynamic processes are still the subject of a recent and active research; see, e.g., Refs. [8–11].

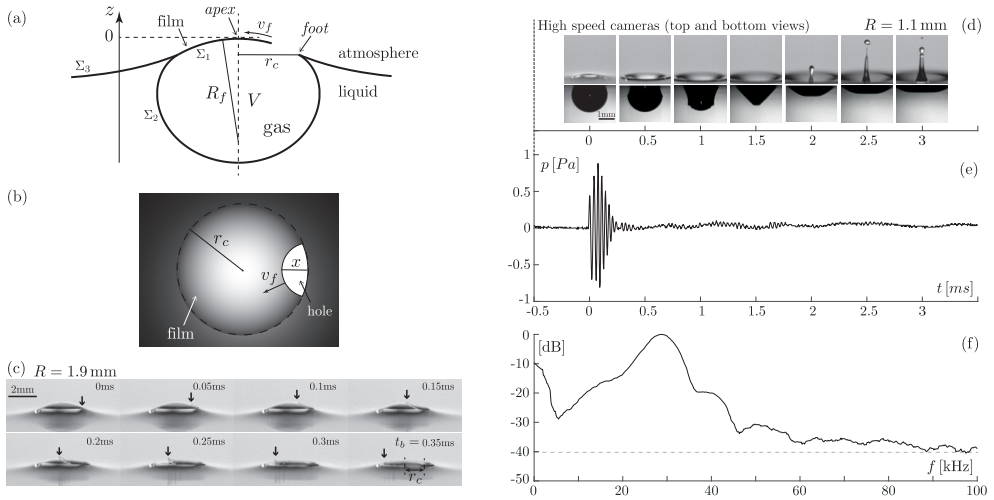


FIG. 2. Sketch of a floating bubble at the initial stage of its collapse corresponding to the retraction of the liquid film: (a) profile view and (b) top view. (c) Sequence of pictures of a floating air bubble with $R = 1.9$ mm equivalent radius viewed from the side above the free water surface, showing the retraction of the water film separating the bubble from the atmosphere. The black arrow indicates the position on the rim of the retracting film. (d) Sequence of pairs of pictures of a $R = 1.1$ mm collapsing air bubble viewed from the side above and below the free water surface using two synchronized high-speed cameras. (e) Synchronized airborne acoustic pressure signal emitted during the collapse and detected using a microphone located 20 mm right above the bubble. (f) Fourier spectrum of pressure signal (dashed line: noise level) (normalized by the maximum of the spectrum).

Here we acquire a high-speed chronophotography of this bubble collapse simultaneously with its emitted acoustic signal. As shown in Fig. 2(e), the bubble emits sound during the first 200 μs after the onset of film retraction. The acoustic emission of capillary bubbles collapsing at a free water surface was studied in Spiel [12] and Deane [13]. Their acoustic emission was interpreted as the transient acoustic emission associated with the free, damped oscillations of a Helmholtz resonator following the instantaneous release of its initial overpressure. The central frequency of the oscillations of the acoustic signal was found to quantitatively agree with the Helmholtz resonator model [12]. It also was observed that the signal emitted by the smallest bubbles ($R < 1$ mm) was chirped [12]. The origin of this phenomenon is still unclear, even if film retraction was speculated to play a role in Spiel [12] and Deane [13], yet without their providing any experimental analysis or data on film retraction. More precisely, Spiel [12] conducted the analysis of the frequency modulation after the end of the film retraction, while Deane [13] indirectly determined the film thickness, key in retraction, from its draining dynamics. Time-resolved imaging of the bubble collapse therefore appears as a mandatory complement to acoustic monitoring to definitively clarify the origin of bubble bursting sound emission.

II. EXPERIMENT

Air bubbles are generated in a parallelepipedal glass tank (20 cm length, 14 cm width, 9.5 cm depth) filled with either tap water or an aqueous solution of SDS (sodium dodecyl sulfate, Sigma Aldrich) surfactant with 2 g/L mass concentration, i.e., $0.9c_{\text{cmc}}$, where c_{cmc} is the critical micellar concentration (see Table I). Bubbles are released from submerged needles connected to a syringe pump filled with air. The needle internal diameters range from 0.08 mm to 1.5 mm. The bubbles rise to the water surface and briefly float before bursting.

Two digital high-speed cameras (Photron SA-5 and Phantom V2511) are used to image the collapsing bubble from the side, one below the free surface, one above it; see Fig. 2(d). The airborne acoustic signature of the bubble collapse is recorded using a Brüel & Kjær 4939-A-011-type microphone with [4 Hz–100 kHz] frequency range at least at 500 kHz sampling frequency. The microphone is positioned at a distance $d = 20$ mm above the free liquid surface, right above the floating bubble, and is oriented vertically downward. The audio and video recordings are synchronized. The acoustic signals are then time shifted by the time of flight of sound between the surface and the microphone, 58 μs . Finally, the acoustic signals are high-pass filtered at a 50 Hz cutoff frequency in order to remove most of the ambient noise principally due to air stream from cameras, electronic devices, and room ventilation. Note that we measured no influence of the tank size on the acoustic signals. Noticeably, each bubble collapse event is thoroughly analyzed so that all the quantities reported in the following figures are extracted from each event.

III. DESCRIPTION OF THE FLOATING BUBBLE

To evaluate the volume V of the floating bubble, we follow the procedure implemented in the work of Ghabache *et al* [9]. First, we image the floating bubble from the side below the surface using a high-speed camera just before the collapse onset. A typical picture of a bubble is shown in Fig. 3(a). The bubble lower hemisphere being regarded as an ellipsoid with vertical symmetry axis, we determine the best fit of its profile by an ellipse with semiminor axis a and semimajor axis b . The bubble volume is assumed to be equal to the volume of the corresponding ellipsoid $V = \frac{4}{3}\pi ab^2$ and the bubble equivalent radius is $R = (ab^2)^{1/3}$. The radii of the studied bubbles range from 0.3 mm to 3 mm.

Since $\text{Bo} \lesssim 1$, floating bubbles are not spherical. Assuming the floating bubbles to be at hydrostatic equilibrium, their shape and altitude are determined by the balance between surface

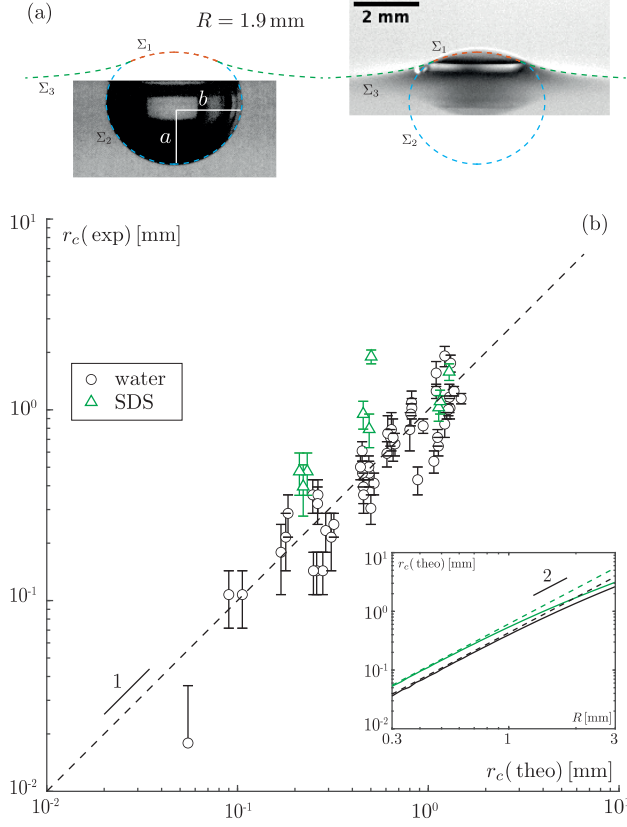


FIG. 3. (a) Pair of pictures from the side below (left) and above (right) the surface of a $R = 1.9$ mm air bubble floating at a water free surface. Σ_1 : liquid film separating the inner air from the atmosphere. Σ_2 : water-air interface below the free surface. Σ_3 : free liquid surface. a (respectively b): semiminor (respectively semimajor) axis of the elliptic best fit of the bottom of the bubble profile. Red (respectively blue, green) dashed curve: shape of Σ_1 (respectively Σ_2 , Σ_3) solution of the Young-Laplace problem (see text). (b) Measured r_c versus their theoretical prediction. The solid line corresponds to the perfect agreement between experiment and theory. Inset: theoretically predicted variation of r_c versus R for pure water (black solid curve) and SDS solution (green solid curve) together with Eq. (5) for pure water (black dashed curve) and SDS solution (green dashed curve).

tension and buoyancy. Floating bubbles display the following features sketched in Fig. 2(a): (1) an ellipsoid-like liquid-gas interface below the free surface, called Σ_2 , and (2) a spherical-shaped liquid film between the gas bubble and the atmosphere at the bubble top, called Σ_1 and having the radius of curvature R_f .

The liquid film being considered as infinitely thin, R_f satisfies the Young-Laplace equation

$$\Delta P = \frac{4\sigma}{R_f}, \quad (2)$$

where ΔP is the air overpressure inside the bubble, considered as homogeneous. When z is the altitude and the film highest point is at altitude $z = 0$ [see Fig. 2(a)], the curvature $\kappa_2(z)$ of the submerged liquid-air interface Σ_2 satisfies

$$\Delta P = \sigma \kappa_2(z) - \rho_l g z, \quad (3)$$

and the curvature $\kappa_3(z)$ of the free surface surrounding the bubble satisfies

$$\sigma \kappa_3(z) - \rho_l g z = 0. \quad (4)$$

The set of Eqs. (2), (3), and (4) constrained by the conditions of fixed air volume V and flat free surface far away from the bubble fully determines ΔP ; it is called hereafter the Young-Laplace problem.

In the $\text{Bo} \ll 1$ limit, capillary effects are predominant over gravity effects. Thus, the pressure in water can be considered as homogeneous across the bubble, and both the upper liquid film and the liquid-gas interface below the free surface can be considered as spherical. Thus, ΔP satisfies two simplified Young-Laplace equations $\Delta P = 4\sigma/R_f$ and $\Delta P = 2\sigma/R$, which result in $R_f = 2R$.

The numerical resolution of the Young-Laplace problem following the method described in the work of Toba [14] using V as input allows us to determine ΔP and the bubble shape, in particular R_f and the radius r_c of the circular edge of the liquid film (Σ_2) viewed from above; see Fig. 3(a). The solution of the Young-Laplace problem, shown in Fig. 3(a), is found to coincide with the bubble profile along Σ_1 , Σ_2 , and Σ_3 . This demonstrates the accuracy of the determination of V using an elliptic fit of the bubble profile. The corresponding variation of r_c versus R for capillary bubbles is shown in the inset of Fig. 3(b). The law proposed in Lhuissier and Villermaux [15] in the $\text{Bo} \rightarrow 0$ limit

$$r_c = \frac{2}{\sqrt{3}} \frac{R^2}{\ell_c} \quad (5)$$

quantitatively fits this curve in the $\text{Bo} \ll 1$ range, as shown in the inset of Fig. 3(b).

To check the validity of this law, we measure r_c by exploiting the pictures of the film opening. Since the rim of the retracting film is clearly visible in these pictures, as shown in Fig. 2(c), its disappearance indicates that it has reached the film edge, whose distance to the bubble axis is equal to r_c . The variations over more than a decade of the experimental values of r_c are compared to their theoretical prediction in Fig. 3(b). Given experimental scatter, a good agreement is observed, which confirms the validity of the model of bubble shape presented in this section.

IV. DYNAMICS OF THE FILM OPENING

In the case of pure water, i.e., surfactant-free films, the lifetime of floating bubbles is very short, usually shorter than 1 s, and the films always break at the bubble foot and not at the apex, as reported in Lhuissier [15] and Champougny [16]. In the case of SDS solutions, the lifetime of floating bubbles is much longer, usually on the order of 1 min, and the film breaking takes place at or close to the bubble top.

We define the film opening duration t_b as the time interval between the picture on which the rim appears at a point located at the bubble foot and the picture on which the rim reaches the diametrically opposed point and disappears; see Fig. 2(c). The variation of t_b versus R for water and SDS solutions is shown in log-log scales in Fig. 4(a). t_b ranges between 10 μs and 500 μs in the investigated range of values of R .

In the case of pure water, since the film breaks at the bubble foot, (1) the hole opening dynamics results from the retraction of a single rim, as sketched in Figs. 2(a) and 2(b) and (2) the film rim travels a total distance equal to $2R_f \arcsin r_c/R_f \simeq 2r_c$, neglecting the film curvature, as shown in Figs. 2(a) and 2(b). The distance x traveled by the rim at time t since film breaking, sketched in Fig. 2(a), is represented in Fig. 4(b) for several values of R . In a first stage, x varies linearly with time, which indicates that the rim retraction velocity is constant and on the order of 10 m s⁻¹. Liquid films with thickness h are known to retract at velocity v_f such that

$$v_f = \sqrt{\frac{2\sigma}{\rho_l h}} \quad (6)$$

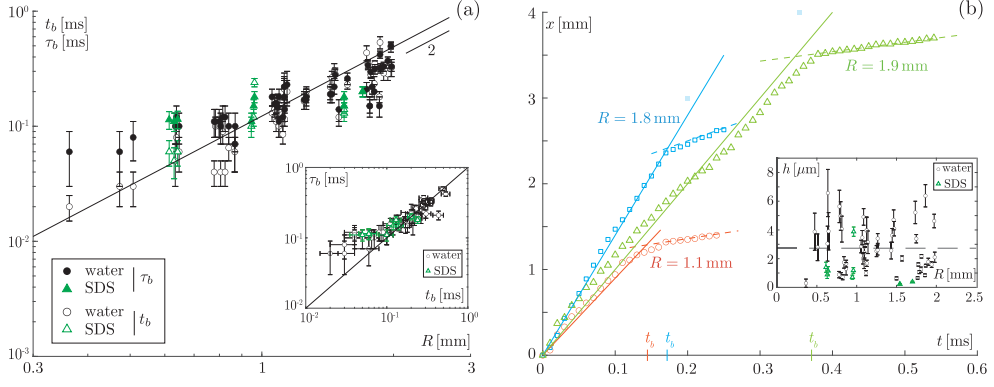


FIG. 4. (a) Measured film opening duration t_b and measured duration τ_b of the frequency chirp of the acoustic emission versus R . Black line: theoretical prediction (8) for t_b corresponding to the average value $\langle h \rangle = 2.7 \mu\text{m}$ of the retracting liquid films. Inset: measured duration τ_b of the frequency chirp of the acoustic emission versus measured film opening duration t_b . (b) Time-dependent distance x traveled since film breaking by the rim (up to t_b), then by the $\Sigma_2 - \Sigma_3$ junction (from t_b) for three different values of R . Lines are best linear fits. Inset: thickness h of the retracting liquid films for the water bubbles deduced from Eq. (6) versus R . Dashed line: average value of h for water bubbles.

as the result of the balance between the inertia of the growing rim and the capillary forces exerted by the liquid film on the rim [17,18]. Since this linear behavior of $x(t)$ is always observed, i.e., $x(t) = v_f t$, we conclude that the thickness h of the spontaneously opening films is always homogeneous. Consequently, h can be deduced from v_f by inverting Eq. (6). The variation of h versus R is shown in the inset of Fig. 4(b). $h(R)$ displays no trend but rather a scatter characterized by a $1.6 \mu\text{m}$ standard deviation around an average value $\langle h \rangle = 2.7 \mu\text{m}$ for water bubbles.

Given that v_f is constant during each film opening, t_b satisfies

$$t_b \simeq \frac{2r_c}{v_f}. \quad (7)$$

Since v_f does not depend on R , in the following we use its average value $\langle v_f \rangle$. By combining Eqs. (5), (6), and (7), we can express t_b as

$$t_b = \frac{4}{\sqrt{6}} \frac{\sqrt{g\langle h \rangle} \rho_l R^2}{\sigma}. \quad (8)$$

This law is represented in Fig. 4(a) for water and SDS solutions [Eq. (6) has been shown to remain valid for retracting films made of SDS solutions as long as $h \geq 0.1 \mu\text{m}$ [19]]. Given the experimental scatter, a good agreement is observed, which confirms the validity of the model of the film opening dynamics presented in this section.

As shown in Fig. 4(b), as soon as $x > 2r_c$, x still varies linearly with time but with a much smaller velocity (on the order of 1 m s^{-1}). This corresponds to the receding motion of the upper edge of the cavity, i.e., to the junction between surfaces Σ_2 and Σ_3 .

In the case of SDS solution, since the film breaks at or close to the bubble top, the hole is circular during most of the opening duration, and consequently the hole diameter, also called x here for simplicity, satisfies $x(t) = 2v_f t$. Thus, $t_b = r_c/v_f$.

These results for the hydrodynamic evolution of a collapsing bubble constitute the background for analyzing its acoustic emission.

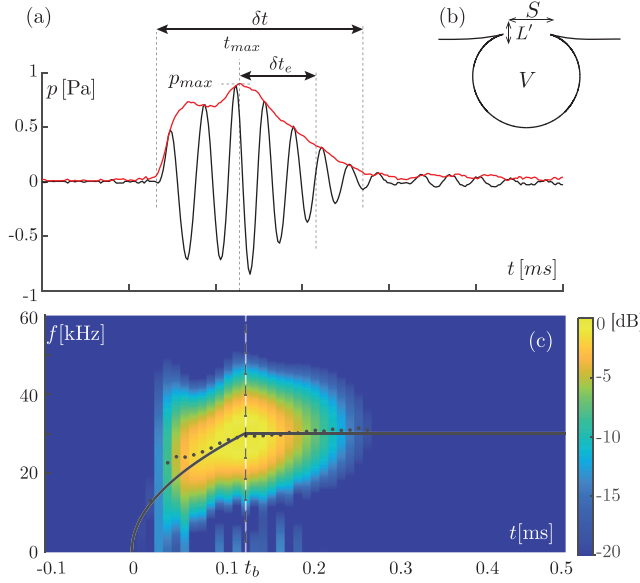


FIG. 5. (a) Airborne acoustic pressure signal emitted during the collapse of a $R = 1.1$ mm air bubble floating at a water free surface. Red curve: absolute value of the Hilbert transform of the signal. (b) Sketch of the opening bubble. (c) Spectrogram of the signal shown in (a). Dots: maxima of the instantaneous spectra. The vertical dashed line indicates the time t_b defined by Eq. (8) at which the film retraction is completed. Black solid curve: prediction of f_H based on Eqs. (11), (13), (12), and (8).

V. ACOUSTIC EMISSION

A. Characteristic features of the acoustic emission

A typical airborne acoustic pressure signal emitted during the collapse of an air bubble floating at the water free surface is shown in Fig. 5(a). The spectrogram of the signal shown in Fig. 5(a) is plotted in Fig. 5(b). We observe that the instantaneous spectra are peak-shaped at all times and that the spectrogram displays two regimes: a first regime during which the corresponding peak frequency f_0 increases with time, i.e., during which the signal is chirped, and a second regime during which f_0 appears as approximately constant.

The variations of f_0 with time for several values of R are represented in log-log scales in Fig. 6(a). In the first regime, f_0 is observed to approximately agree with a $t^{1/2}$ scaling law, while in the second regime, f_0 increases much more slowly. We define τ_b as the time at which the transition between the two regimes occurs; see Fig. 6(a). τ_b is called the chirp duration hereafter. The variation of τ_b with R is represented in Fig. 4(a). In the inset we also compare τ_b with the film opening duration t_b . t_b is observed to coincide with τ_b for bubbles larger than 0.5 mm given the experimental scatter. This demonstrates that the chirp is correlated with the film opening. Moreover, the influence of the bubble geometry on its acoustic emission has to be questioned.

B. Helmholtz's resonator model

In the works of Spiel [12] and Deane [13], the acoustic emission of collapsing bubbles was modeled using Helmholtz's model of airborne radiation of an open cavity [20]. According to this lumped-element model of open acoustic resonator, a cavity with volume V communicating with the atmosphere through an bottleneck-like aperture with area S and length L behaves as a mass-spring harmonic oscillator whose inertia is associated to the mass of the air column oscillating in the cavity

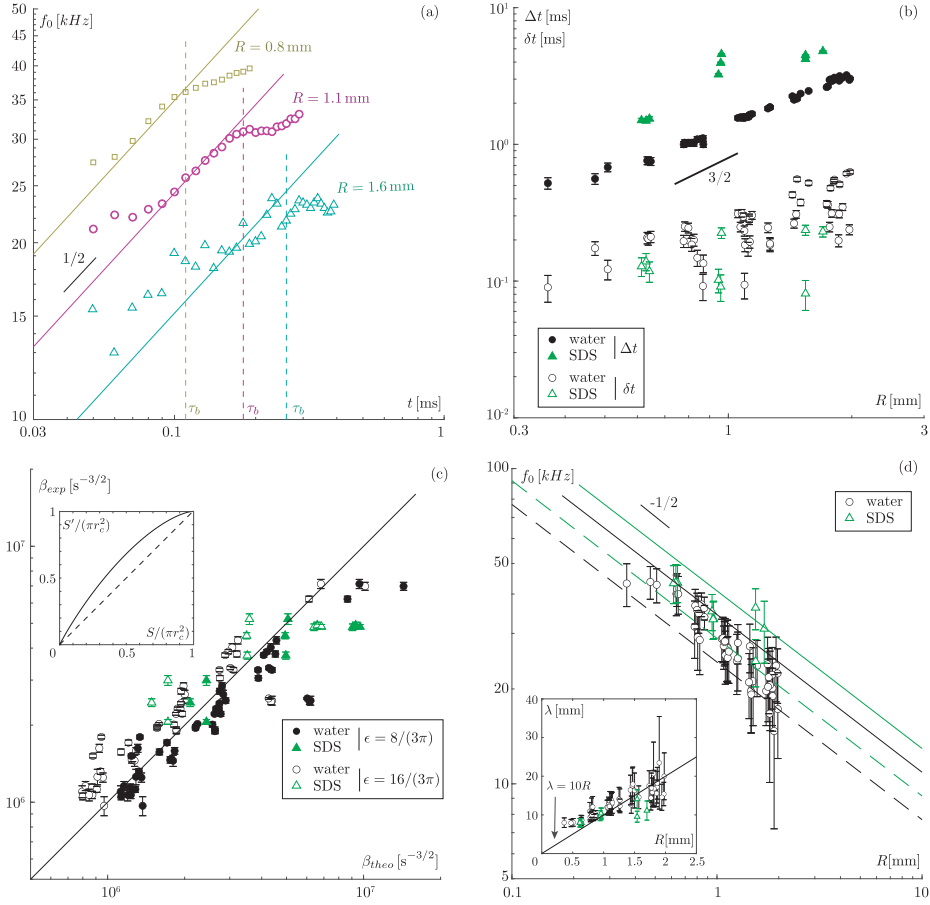


FIG. 6. (a) Time-dependent peak frequency $f_0(t)$ of the instantaneous spectra of the airborne acoustic emission of collapsing bubbles for three different values of the bubble equivalent radius R . (b) Measured duration δt of the acoustic signal and duration of the bubble collapse Δt . Solid line: scaling law for Δt from [9]. (c) Prefactor of the scaling law $f_H = \beta_{exp} t^{1/2}$ as a function of its theoretical prediction β_{theo} using by Eq. (12). The solid line corresponds to the perfect agreement between experiment and theory. Inset: Variation of the section S' , defined in Eq. (10), over the variation of area S defined for a circular hole. (d) Variation versus R of the peak frequency $f_0(t_b)$ of the instantaneous spectra of the airborne acoustic emission of collapsing bubbles at the instant t_b at which the liquid film opening is ending. Black line (respectively dashed line): theoretical prediction (13) with $\epsilon = 8/(3\pi)$ [respectively $\epsilon = 16/(3\pi)$]. Inset: acoustic wavelength λ versus R . Solid line: law $\lambda = 10R$.

aperture and whose stiffness is associated to the compressibility of the air enclosed in the cavity. The corresponding oscillator resonant frequency f_H is such that

$$f_H = \frac{c}{2\pi} \sqrt{\frac{S}{L'V}}, \quad (9)$$

where c is the speed of sound in the gas, $L' = L + \epsilon r$ the length of the air column oscillating in the cavity aperture, r the radius of the aperture regarded as circular, and ϵ a dimensionless parameter reflecting the nonlinear air flow inside and outside the aperture, typically $\epsilon = 8/(3\pi)$ in the case of a non-baffled resonator and $16/(3\pi)$ in the case of a baffled resonator [20]. This model can in

principle be applied to a collapsing bubble by considering that the cavity corresponds to the bubble volume and the aperture to the hole in the liquid film, both varying during the collapse.

Since the cavity starts collapsing during its acoustic emission, we might wonder if the bubble volume can be assumed as constant during the bubble acoustic emission. To answer this question, we compare the duration of the acoustic emission δt to the collapse duration Δt . Δt is defined as the time elapsed between the hole nucleation and the cavity reversal [i.e., when the depth of the immersed cavity starts to increase, close to 1.5 ms in Fig. 2(d)]. The variation of Δt versus R is plotted in Fig. 6(b). We observe that Δt scales approximately as $R^{3/2}$, in agreement with the scaling law $\Delta t \sim \sqrt{\rho R^3 / \sigma}$ describing the inertial collapse of the cavity driven by surface tension [9]. Δt increases when SDS-surfactant is used because Δt scales as $\sigma^{-1/2}$ and σ is lower in presence of surfactant. On the other hand, δt is defined as the time elapsed during which the amplitude of the Hilbert transform of the pressure signal is larger than $p_{\max}/10$, where p_{\max} is the maximum of the Hilbert transform; see Fig. 5(a). The variation of δt versus R is plotted in Fig. 6(b). We observe that $\delta t < \Delta t$ in the whole range of the investigated values of R (interestingly, δt exhibits a large dispersion, but the upper boundary of the data exhibits the same scaling as Δt). We conclude that the acoustic emission proceeds and ends at the very beginning of the bubble collapse. Consequently, we can safely assume the bubble volume to be constant and equal to its initial volume V during its acoustic emission.

Due to the geometry of the opening bubble sketched in Fig. 5(a), the length L of the resonator aperture can be taken equal to zero. In the case of surfactant-free water, since the liquid film breaks at the bubble foot, the hole is not circular, as sketched in Fig. 5(b). Therefore, we cannot straightforwardly define an equivalent aperture radius r . But the area S' of a hole with width x ,

$$S' = 2 \left[\frac{x^2}{2} \arccos \left(\frac{x}{2r_c} \right) + r_c^2 \arcsin \left(\frac{x}{2r_c} \right) \right] - x \sqrt{r_c^2 - \left(\frac{x}{2} \right)^2}, \quad (10)$$

is not very different from the area $S = \pi(x/2)^2$ of a circular hole with radius $x/2$, as shown in the inset of Fig. 6(c). Consequently, in the following we approximate S' by S , and we assume the equivalent aperture radius r associated to the film hole to equal $x/2$ and $L' \simeq \varepsilon x/2$.

With these approximations, the resonant frequency f_H of the acoustic emission of the collapsing bubble satisfies

$$f_H(t) = \beta_{\text{theo}} t^{1/2} \text{ for } t \leq t_b \quad (11)$$

with

$$\beta_{\text{theo}} = \frac{c}{4\pi} \sqrt{\frac{3v_f}{2\varepsilon R^3}}. \quad (12)$$

Noticeably, at $t = t_b$,

$$f_H(t_b) = \beta_{\text{theo}} t_b^{1/2} = \frac{c}{4\pi} \sqrt{\frac{2\sqrt{3}}{\varepsilon \ell_c R}}. \quad (13)$$

According to Eq. (11), $f_H \propto t^{1/2}$, which is in agreement with the experimental observation that $f_0 \propto t^{1/2}$. To quantitatively test the validity of Eq. (11), we determine the best fit of $f_0(t)$ by the function $\beta_{\text{exp}} t^{1/2}$ with β_{exp} as free parameter; see Fig. 6(a). The variation of β_{exp} as function β_{theo} computed using $\varepsilon = 8/(3\pi)$ and $\varepsilon = 16/(3\pi)$ are plotted in Fig. 6(c). Given the experimental scatter, a satisfactory correlation between β_{exp} and β_{theo} is observed whatever the value of ε , which demonstrates the validity of Eq. (11).

To conclude this study of the first regime, we point out that combining high-speed imaging and time-frequency analysis, we have demonstrated that Helmholtz's model applied to the bubble assumed as preserving its initial volume quantitatively describes the measured frequency chirp provided that the film opening dynamics is taken into account. As an illustration of the accuracy

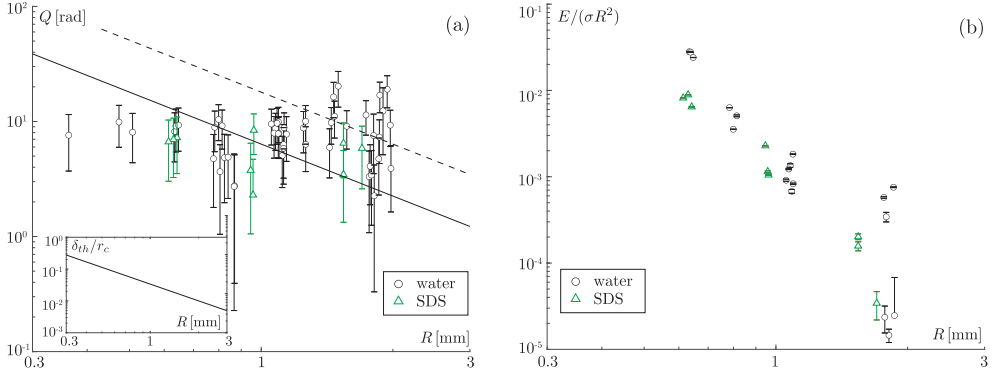


FIG. 7. (a) Measured quality factor Q versus R . Solid line (respectively dashed line): theoretical prediction Eq. (16) computed using $\delta = 8/(3\pi)$ (respectively $\delta = 16/(3\pi)$). Inset: theoretical ratio of the characteristic thermal length to hole radius as function of bubble radius. (b) Dimensionless radiated acoustic energy $E/(\sigma R^2)$ versus R .

of this theoretical description of the bubble acoustic emission, we have superimposed on the spectrogram shown in Fig. 5(c) the prediction of f_H based on Eqs. (11), (13), and (8), which involves no free parameter.

As a final remark, we note that in the second regime (after τ_b) f_0 actually still increases but much more slowly than in the first regime, as shown in Fig. 6(a). Following Spiel [12], we attribute this slower chirp to the recession of the upper edge of the cavity, which is much slower (an order of magnitude less) than the film opening, as shown in Fig. 4(b).

Next, we test the quantitative validity of Eq. (11) by plotting the variation versus R of f_0 measured at the end of the chirp [i.e., at $t = \tau_b$; see Fig. 6(a)] versus $f_H(t_b)$ defined by Eq. (13) and computed using $\varepsilon = 8/(3\pi)$ and $\varepsilon = 16/(3\pi)$. Given the experimental scatter, a good agreement between $f_0(\tau_b)$ and $f_H(t_b)$ is observed. For $R < 1$ mm, $\varepsilon = 8/(3\pi)$ results in a quantitative agreement with the measurements. These results are consistent with the results of the work of Spiel [12] (see Fig. 7 in Ref. [12]). Interestingly, Eqs. (1), (13) constitute a closed-form, valid expression for the f_H - V relationship that can be applied to any liquid-gas system.

Finally, reminding that a lumped-element model of acoustic resonator is valid only for subwavelength resonators; i.e., for $R/\lambda \ll 1$, we aim to test the consistency of Helmholtz's model of open resonator applied to the collapsing bubble. The variation of λ versus R is plotted in the inset of Fig. 6(d). We observe that $\lambda \gg R$ in the entire range of investigated values of R , which *a posteriori* justifies the use of Helmholtz's model.

C. Quality factor

The acoustic signal can also be characterized by its duration and its amplitude. Here we focus on the second regime of the acoustic emission and in particular on the characteristic timescale of decrease of the signal amplitude. Assuming a linear relaxation of the free pressure oscillations in the acoustic resonator, we expect the pressure signal to satisfy $p(t) = p_{\max} \exp(-t/\tau) \cos(\omega_0 t + \phi)$, where $\omega_0 = 2\pi f_0$. τ can be experimentally evaluated as being equal to the laps δt_e between the instant t_{\max} at which p reaches its maximum p_{\max} and the instant at which its envelope reaches p_{\max}/e ; see Fig. 5(b). The quality factor Q of the resonator can be deduced from τ through

$$Q = \frac{1}{2} \omega_0 \tau. \quad (14)$$

The variation of Q deduced from Eq. (14) versus R is plotted in Fig. 7(a). Interestingly, the upper boundary of the data is horizontal, corresponding to $Q \simeq 10$. According to Ref. [20], under

the assumption of negligible thermo-viscous dissipation, the quality factor Q of the resonator is predicted to satisfy

$$Q = 2\pi\sqrt{\frac{L^3V}{S^3}}. \quad (15)$$

Using the same assumptions as above for adapting Helmholtz's model to the opening bubble, Q has the following expression:

$$Q = 2\pi\sqrt{\varepsilon^3 \frac{\sqrt{3}}{2\pi} \frac{\ell_c^3}{R^3}}. \quad (16)$$

The smaller Q , the shorter the acoustic emission. Figure 6(b) shows δt is smaller when SDS surfactant is used. To qualitatively explain this, we note that Q increases with ℓ_c as $\ell_c^{3/2}$ [see Eq. (16)] and that ℓ_c increases with σ as $\sigma^{1/2}$. Thus, the lower the surface tension, the smaller Q . Equation (16) computed using $\varepsilon = 8/(3\pi)$ and $\varepsilon = 16/(3\pi)$ is plotted in Fig. 7(a). We observe that the experimental data do not agree with the theoretical prediction, particularly for small values of R , except as regards the order of magnitude. We believe that the thermo-viscous dissipation occurring in the vicinity of the neck may explain the observed discrepancy. As shown in the inset of Fig. 7(a), the characteristic thermal length/thermal boundary layer thickness $\delta_{\text{th}} = \sqrt{2D_{\text{th}}/\omega}$ ($D_{\text{th}} = 2 \times 10^{-5} \text{ m}^2 \text{ s}^{-1}$ is the thermal diffusivity of air) is indeed close to r_c in the experimentally investigated range of values of R , particularly for small values of R . The same considerations hold for the characteristic viscous length/viscous boundary layer thickness $\delta_v = \sqrt{2\nu/\omega}$ ($\nu = 1.5 \times 10^{-5} \text{ m}^2 \text{ s}^{-1}$ is the kinematic viscosity in air at ambient temperature).

D. Radiated acoustic energy

Since a collapsing bubble radiates sound that is characterized by a wavelength much larger than the bubble aperture, diffraction tends to scatter sound in all directions, and the microphone lies in the far field of the bubble ($d \gg z$, where $z \approx r_c^2/2\lambda$ is the Rayleigh distance). Thus, following the work of Divoux [21], we can assume an acoustic radiation with spherical symmetry, and the total acoustic energy E can be computed from the pressure signal $p(t)$ using

$$E = \frac{2\pi d^2}{\rho_g c} \int_0^\infty p^2(t) dt. \quad (17)$$

Noting that the acoustic radiation originates from the sudden release of Laplace overpressure $\Delta P \simeq 2\sigma/R$, we assume that E is bounded by the energy stored in the floating bubble which scales as σR^2 . The variation of $E/(\sigma R^2)$ versus R is plotted in Fig. 7(b). We observe that $E/(\sigma R^2)$ strongly decreases with R .

VI. CONCLUSION

Let us summarize our results. Once a rising gas bubble has arrived at a free liquid surface, the liquid film separating the inner gas from the atmosphere drains and finally breaks when its thickness reaches a few micrometers, in absence or in presence of surfactants. The airborne acoustic emission associated with the release of the Laplace overpressure and the film opening start simultaneously. The frequency content of the resulting signal can be quantitatively explained using Helmholtz's model of an open resonator exhibiting a sequence of two regimes: (1) a first episode during which the liquid film opens and the resonator eigenfrequency drifts correspondingly (frequency chirp) and (2) a second regime characterized by a nearly constant oscillation eigenfrequency and a decreasing amplitude. At the end of the bubble acoustic emission, the liquid cavity has barely initiated its collapse. Interestingly, the acoustic emission of bubbles with radius smaller than 1.5 mm in water is audible in the first regime and is ultrasonic in the second regime.

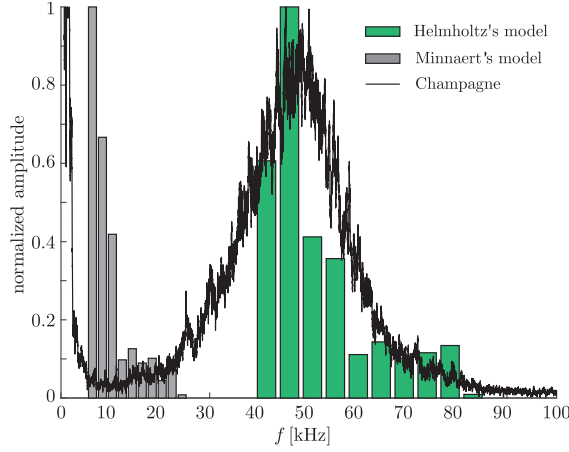


FIG. 8. Black solid curve: acoustic spectrum of the 1 s duration airborne acoustic recording above a glass of champagne. Green bars: histogram of the resonant frequency of acoustic emission of the floating bubbles whose histogram of radii is shown. Figure 1(b) predicted using Helmholtz’s model of open resonator Eq. (13). Gray bars: histogram of the resonant frequency of acoustic emission of the floating bubbles predicted using Minnaert’s model of open resonator (18).

Let us now come back to the champagne effervescence. Neglecting the first regime characterized by a frequency chirp, we can compute the central frequency of the acoustic emission of a collapsing champagne bubble with radius R using Helmholtz’s model of an open resonator Eq. (13) and the values of density and surface tension of champagne and of sound speed in CO_2 given in Table I. From the histogram of the radii of floating champagne bubbles shown in Fig. 1(b), we can compute the histogram of the corresponding acoustic resonant frequency, which is shown in Fig. 8. We note that this histogram quantitatively fits the acoustic peak-shaped spectrum of airborne acoustic emission of champagne except along its low-frequency tail. Moreover, both the average frequency of the histogram $\langle f_H \rangle = 53 \text{ kHz}$ and the frequency of its maximum coincide with the spectrum average frequency. Since the first regime of acoustic emission is characterized by frequencies smaller than those predicted using Eq. (13), we expect the low-frequency tail of the spectrum to correspond to the first regime that is precisely not modeled here. We stress that in the case of champagne most of the acoustic energy is in the ultrasonic regime.

We conclude that we have modeled the frequency content of the airborne acoustic emission of gas bubbles collapsing at a free liquid surface and in particular of champagne and sparkling liquids. When the film is completely retracted, we highlighted a closed-form expression of the resonance frequency at this time involving only one single geometric parameter, the gas volume. We believe that this quantitative description could be used to synthesize artificial acoustic signals of digital animation films as in the work of Langlois *et al.* [22].

According to Minnaert [23], subsurface gas bubbles undergoing volume oscillations are known to emit sound. The resonant frequency f_M of their small amplitude, harmonic volume oscillations satisfies

$$f_M = \frac{1}{2\pi R} \sqrt{\frac{3\gamma P_0}{\rho_\ell}}, \quad (18)$$

where γ is the gas adiabatic index ($\gamma = 1.3$ for CO_2) and P_0 the atmospheric pressure. This equation is used to determine the radius distribution of submerged oscillating bubbles from the acoustic spectrum in studies of sparkling liquids [6], of the breaking of waves [24,25], or of the sound emission of rain impact [26].

Actually, the process of airborne acoustic emission accompanying the bubble collapse markedly differs from Minnaert’s model of acoustic emission of subsurface bubbles undergoing volume oscillations [23]. Consequently, f_M markedly differs from f_H . To illustrate this, we have computed the histogram of the acoustic resonant frequency using Eq. (18) from the histogram of the radii of floating champagne bubbles shown in Fig. 1(b). It is plotted in Fig. 8. We note that this histogram, whose average frequency is $\langle f_M \rangle = 11$ kHz, corresponds to a trough in the spectrum of airborne acoustic emission of champagne. We conclude that this mechanism of sound radiation does not contribute to the airborne acoustic emission of champagne.

More generally, this work is a step in understanding the acoustic signature of violent hydrodynamic events, which adds to previous studies on volcano eruptions [21,27,28], impacts on liquid surfaces by droplets [26] or solid spheres [29], breaking waves [24,25], and bursting soap bubbles [30]. We believe that the analysis of the acoustic signature of such fast and violent hydrodynamic events should provide information, complementary to high-speed imaging, on the main flow features, on the forces at play, and on the relying physical processes.

ACKNOWLEDGMENT

We thank Caroline Derec, Valentin Leroy and Adrien Bussonnière for fruitful discussions.

-
- [1] G. Liger-Belair, The physics and chemistry behind the bubbling properties of Champagne and sparkling wines: A state-of-the-art review, *J. Agri. Food Chem.* **53**, 2788 (2005).
 - [2] G. Liger-Belair *et al.*, Unraveling different chemical fingerprints between a champagne wine and its aerosols, *Proc. Natl. Acad. Sci. USA* **106**, 16545 (2009).
 - [3] G. Liger-Belair, T. Séon, and A. Antkowiak, Collection of collapsing bubble driven phenomena found in champagne glasses, *Bubble Sci., Eng. Technol.* **4**, 21 (2012).
 - [4] E. Ghabache, G. Liger-Belair, A. Antkowiak, and T. Séon, Evaporation of droplets in a Champagne wine aerosol, *Sci. Rep.* **6**, 25148 (2016).
 - [5] G. Liger-Belair *et al.*, Kinetics of gas discharging in a glass of champagne: The role of nucleation sites, *Langmuir* **18**, 1294 (2002).
 - [6] K. Spratt, K. Lee, and P. Wilson, Champagne acoustics, *Phys. Today* **71**(8), 66 (2018).
 - [7] R. Span and W. Wagner, A new equation of state for carbon dioxide covering the fluid region from the triple-point temperature to 1100 K at pressures up to 800 MPa, *J. Phys. Chem. Ref. Data* **25**, 1509 (1996).
 - [8] L. Duchemin, S. Popinet, C. Josserand, and S. Zaleski, Jet formation in bubbles bursting at a free surface, *Phys. Fluids* **14**, 3000 (2002).
 - [9] E. Ghabache, A. Antkowiak, C. Josserand, and T. Séon, On the physics of fizziness: How bubble bursting controls droplets ejection, *Phys. Fluids* **26**, 121701 (2014).
 - [10] L. Deike, E. Ghabache, G. Liger-Belair, A. K. Das, S. Zaleski, S. Popinet, and T. Seon, Dynamics of jets produced by bursting bubbles, *Phys. Rev. Fluids* **3**, 013603 (2018).
 - [11] A. Gañán-Calvo, Revision of Bubble Bursting: Universal Scaling Laws of Top Jet Drop Size and Speed, *Phys. Rev. Lett.* **119**, 204502 (2017).
 - [12] D. Spiel, Acoustical measurements of air bubbles bursting at a water surface: Bursting bubbles as Helmholtz resonators, *J. Geophys. Res.* **97**, 11443 (1992).
 - [13] G. Deane, Determining the bubble cap film thickness of bursting bubbles from their acoustic emissions, *JASA* **133**, EL69 (2013).
 - [14] Y. Toba, Drop production by bursting of air bubbles on the sea surface: (II) Theoretical study on the shape of floating bubbles, *J. Oceanogr. Soc. Jpn.* **15**, 121 (1959).
 - [15] H. Lhuissier and E. Villermaux, Bursting bubble aerosols, *JFM* **696**, 5 (2012).
 - [16] L. Champougny, M. Roché, W. Drenckhan, and E. Rio, Life and death of not so “bare” bubbles, *Soft Matter* **12**, 5276 (2016).

- [17] G. Taylor, The dynamics of thin sheets of fluid. III. Disintegration of fluid sheets, [Proc. R. Soc. London A](#) **253**, 313 (1959).
- [18] F. Culick, Comments on a ruptured soap film, [J. Appl. Phys.](#) **31**, 1128 (1960).
- [19] W. McEntee and K. Mysels, Bursting of soap films. I. An experimental study, [J. Phys. Chem.](#) **73**, 3018 (1969).
- [20] L. Kinsler, A. Frey, A. Coppens, and J. Sanders, *Fundamentals of Acoustics*, 4th ed. (Wiley, New York, 2000).
- [21] T. Divoux, V. Vidal, F. Melo, and J.-C. G  minard, Acoustic emission associated with the bursting of a gas bubble at the free surface of a non-Newtonian fluid, [Phys. Rev. E](#) **77**, 056310 (2008).
- [22] T. R. Langlois, C. Zheng, and D. L. James, Toward animating water with complex acoustic bubbles, [ACM Trans. Graphics \(TOG\)](#) **35**, 95 (2016).
- [23] M. Minnaert, On musical air-bubbles and the sounds of running water, [Lon. Edinb. Dublin Philos. Mag. J. Sci.](#) **16**, 235 (1933).
- [24] K. Bolin and M.   bom, Air-borne sound generated by sea waves, [JASA](#) **127**, 2771 (2010).
- [25] G. Deane and M. Stokes, Scale dependence of bubble creation mechanisms in breaking waves, [Nature \(London\)](#) **418**, 839 (2002).
- [26] A. Prosperetti and H. Oguz, The impact of drops on liquid surfaces and the underwater noise of rain, [Annu. Rev. Fluid Mech.](#) **25**, 577 (1993).
- [27] S. Vergn  lle, M. Boichu, and J. Caplan-Auerbach, Acoustic measurements of the 1999 basaltic eruption of Shishaldin volcano, Alaska: 1. Origin of Strombolian activity, [J. Volcanol. Geotherm. Res.](#) **137**, 109 (2004).
- [28] V. Vidal *et al.*, Dynamics of soap bubble bursting and its implications to volcano acoustics, [Geophys. Res. Lett.](#) **37**, L07302 (2010).
- [29] C. D  uez, C. Ybert, C. Clanet, and L. Bocquet, Making a splash with water repellency, [Nat. Phys.](#) **3**, 180 (2007).
- [30] A. Bussonni  re, A. Antkowiak, F. Ollivier, M. Baudoin, and R. Wunenburger, Acoustic Sensing of Forces Driving Fast Capillary Flows, [Phys. Rev. Lett.](#) **124**, 084502 (2020).